JOURNAL OF PROPULSION AND POWER
Vol. 9, No. 1, Jan.–Feb. 1993

Gas-Dynamic Flow in a Spinning, Coning Solid Rocket Motor

D. L. Misterek,* J. W. Murdock,† and S. Koshigoe‡
Aerospace Corporation, El Segundo, California 90245

A numerical study was performed to calculate the moment induced by gas-dynamic flow through a spinning, coning payload assist module (PAM). Although the flow is three-dimensional, the solution is achieved by solving two sets of two-dimensional equations. The flowfield in a spinning, nonconing motor is first obtained. Then, the spatially periodic perturbation about the axisymmetric flow is computed to account for the vehicle's coning motion. Inviscid, single-phase simulations were performed with geometries corresponding to the grain configurations near the beginning, middle, and end of the burn. For all cases a stabilizing moment is predicted. However, the numerical study predicts a moment that is only 40–80% of the commonly used jet-damping value obtained from a one-dimensional flow theory. The simulations using the two earlier grain configurations agree with flight data; the vehicle exhibits stable motion for approximately the first three-quarters of the firing. However, the analysis for the grain configuration near the end of burn predicts stability but an exponential increase in the cone angle is observed in flight. The model was improved by including the aluminum oxide particles and viscous effects separately. The two-phase flow calculation predicts a slightly larger stabilizing moment than the inviscid solution. The predicted moment for the turbulent simulation is nearly equal to that calculated in the inviscid analysis. These simulations indicate that gas-dynamic flow is not the cause of the instability observed on the PAM.

I. Introduction

VIRTUALLY all spin-stabilized vehicles consisting of a satellite and a payload assist module (PAM) upper stage have exhibited a relatively consistent precessional instability (coning) near the end of the motor burn. Flight data displaying this typical behavior is shown in Fig. 1 where the pitch rates for three vehicles using PAM motors are presented. For about the first 55 s of the firing, the amplitude of the transverse rate is seen to remain small, indicating the vehicle coning motion is either being damped or, at least, not growing. After about 55 s, an exponential instability sets in and lasts for the remainder of the burn. Although such coning did not prevent these missions from being successful, it has resulted in the use of a so-called nutation control system on some flights. To date, the actual cause of the coning or precessional growth is unknown.

One possible cause is the gas-dynamic flow through the motor. The jet-damping model of gas flow through a spinning, precessing motor predicts the presence of a moment on the vehicle which will decrease the cone angle.[1] This damping moment is the reason vehicles are spin-stabilized and arises from the interaction of an implicitly assumed one-dimensional, gas-dynamic flow with the Coriolis force. The flow through the PAM motor is far from one-dimensional, as this class of motors (Fig. 2) has the nozzle pushed forward so that it is embedded in a nearly spherical combustion chamber. Hence, the gas-induced moment for the PAM motor could be substantially different than the jet-damping moment.

We are aware of two separate groups which have investigated the changes to the moment for non-one-dimensional flows. Both groups began by studying flows in precessing vehicles with simple analytical models and then proceeded to numerical simulations.

Meyer[2] performed the initial work for the group into which the present work falls. He showed that with the proper choice of coordinate systems, the flow through a spinning, coning vehicle is steady. Meyer also formulated a model problem consisting of the inviscid, incompressible flow through a cylinder. His solution to this model problem contained some mathematical errors which were corrected in a subsequent work by Murdock and Meyer.[3] The analytical solutions presented in their report showed that although the geometry considered is one-dimensional, the moments predicted by the three-dimensional flow model agree with the jet-damping values only at large Rossby numbers. At small Rossby numbers,

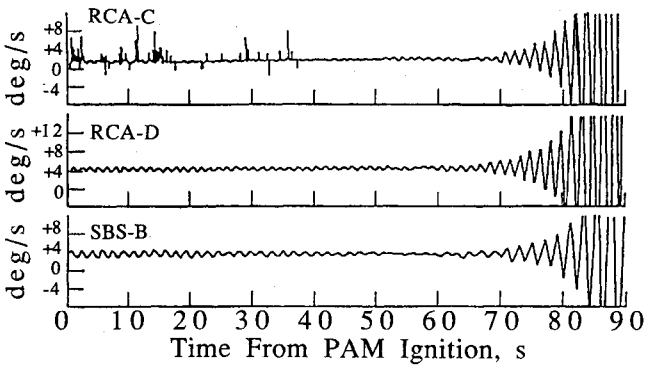

Fig. 1 Pitch rate data from PAM flights.

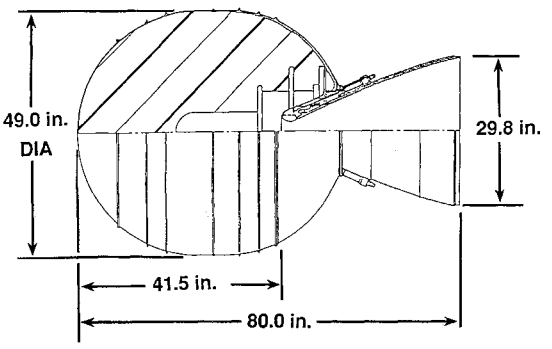

Fig. 2 PAM motor geometry.

Presented as Paper 91-1671 at the AIAA 22nd Fluid Dynamics, Plasma Dynamics and Lasers Conference, Honolulu, HI, June 24–26, 1991; received Oct. 7, 1991; revision received June 8, 1992; accepted for publication June 11, 1992. This paper is declared a work of the U.S. Government and is not subject to copyright protection in the United States.

*MTS, Thermodynamic Technology Section. Member AIAA.
†Manager, Fluid Mechanics Technology Section. Associate Fellow AIAA.
‡MTS, Fluid Mechanics Technology Section. Member AIAA.

although the precession angle is still damped, the damping moment varies strongly with cylinder length. The work also concludes that the stability of a spinning vehicle propelled by a rocket motor can only be predicted from a numerical simulation. The present work performs this type of analysis.

As for the other group, Flandro et al.,[4,5] considered a somewhat more complicated incompressible model problem than the one described in the previous paragraph. Their solution indicates that precessional instabilities are possible under certain conditions. However, Murdock and Meyer[3] suggest that Ref. 4 failed to solve a well-posed boundary value problem and, hence, the conclusion that gas-dynamic instabilities are possible requires independent confirmation. This group has also proceeded from analytical to numerical approaches; work similar to that described here has been initiated by Roach, et al.[6] At this time only swirling axisymmetric flows have been computed and so no statement about stability can be made; however, they indicated they plan to compute the full three-dimensional flow in a spinning, precessing motor. As discussed in the following paragraphs, their proposed approach to the three-dimensional flow problem differs from ours.

The formulation of the numerical problem solved herein is described in Sec. II. The approach is novel in that rather than numerically solving the full three-dimensional flow equations, we solve two sets of two-dimensional equations derived by linearizing in the cone angle. The numerical techniques are based on a two-dimensional, finite-volume, total variation diminishing (TVD) method developed by Wang[7] and are described in Sec. III. Numerical results of increasing complexity are presented in Secs. IV–VI. Section IV summarizes the solutions to the inviscid equations. In Sec. V the effect of adding aluminum oxide particles to the inviscid flow is discussed. In Sec. VI the viscous, single-phase flow calculations are presented.

II. Formulation

The goal of the present work is to calculate the internal pressure field in a PAM motor which is spinning and coning. Given this pressure field, the moments acting on the vehicle due to the flow can be obtained by integrating over the inner surface. Conceptually, the simplest way to obtain this pressure field is to numerically solve for the three-dimensional flow in the motor geometry of interest. This approach has two disadvantages. The first disadvantage is that the side force causing the moment is very small compared with the motor thrust, and hence, the flow is nearly axisymmetric. This means that any three-dimensional numerical scheme must be very accurate in order to resolve the small, nonaxisymmetric part of the flow. The second disadvantage of a three-dimensional flow solution is its cost. The PAM motor combustion chamber near the end of burn is very large and the flow velocities are small, on the order of 10 ft/s. Hence, the chamber has a relatively long characteristic time. By contrast, the nozzle throat has flow velocities of several thousand feet per second and a length scale (diameter) an order of magnitude smaller than that of the combustion chamber. The disparate time scales (length/velocity) associated with these two regions result in very long computing times, even for a two-dimensional calculation. (The short numerical time steps set by the flow in the throat result in a requirement of tens of thousands of time steps to converge the combustion chamber flow.) The long computing times are, of course, exacerbated by the necessity to perform a three-dimensional computation.

To obviate these problems, we have chosen to implement the analytical technique used by Meyer[2] and Murdock and Meyer[3] to treat a model problem. They first solve for the axisymmetric spinning flow (the zero-order flow), which neglects the coning or precession of the vehicle. Then, the linear perturbation to this flow (the first-order flow) is obtained for small cone angle. Both of these flowfields may be obtained with a two-dimensional flowfield code: the zero-order flow is steady and axisymmetric, and the first-order flow is steady in the precessional reference frame and periodic in the azimuthal angle. The accuracy problem is eliminated by obtaining the perturbation to the axisymmetric flow as a separate solution. Thus, no matter how small it is, the perturbation will not be lost in the noise of the basic solution. The computer run-time problem is mitigated because it is easier to obtain two two-dimensional solutions rather than one three-dimensional solution.

To be completely accurate, the gas-dynamic coning problem is a coupled problem in which the Euler dynamical equations for the solid body should be solved simultaneously with the fluid flow equations. As discussed in Refs. 2 and 3, we assume that the quasisteady flow in the motor is determined by the instantaneous spin and precession rate of the vehicle. In turn, the gas-dynamic moment is that obtained by integrating the quasisteady pressure field. Such decoupling of the dynamics can be justified by the fact that the flow time through the motor is small compared to the experimentally observed time scale for cone angle change. Similarly, the burn surface geometry changes on a long time scale compared with the flow time scale. Hence, we solve the steady flow equations for a given burn surface geometry, and then integrate the pressure to find the forces and moments acting on the vehicle.

Figure 3 defines the coordinate system. The X-Y-Z space is inertial space, whereas xyz is the noninertial frame of interest. The coordinate system is oriented such that Z aligns with the flight path and z aligns with the vehicle's primary axis. The x-y plane is precession-fixed, not body-fixed. The angle θ is the cone angle, and ψ and φ are the other two Euler angles. The angular velocity in the x-y-z frame is

$$\boldsymbol{\omega} = \frac{\mathrm{d}\theta}{\mathrm{d}t}\boldsymbol{i}_x + \frac{\mathrm{d}\psi}{\mathrm{d}t}\sin\theta\boldsymbol{i}_y + \frac{\mathrm{d}\psi}{\mathrm{d}t}\cos\theta\boldsymbol{i}_z \tag{1}$$

The solid-body gyroscope equations (Euler's equations) governing the axisymmetric vehicle take the usual form, even though the transverse and longitudinal moments of inertia, I and I_z, are time varying[2]:

$$M_x = I\left[\frac{\mathrm{d}^2\theta}{\mathrm{d}t^2} - \left(\frac{\mathrm{d}\psi}{\mathrm{d}t}\right)^2\sin\theta\cos\theta\right] + I_z\frac{\mathrm{d}\psi}{\mathrm{d}t}\sin\theta\left(\frac{\mathrm{d}\psi}{\mathrm{d}t}\cos\theta + \frac{\mathrm{d}\varphi}{\mathrm{d}t}\right) \tag{2a}$$

$$M_y = I\left(\frac{\mathrm{d}^2\psi}{\mathrm{d}t^2}\sin\theta + 2\frac{\mathrm{d}\psi}{\mathrm{d}t}\frac{\mathrm{d}\theta}{\mathrm{d}t}\cos\theta\right) - I_z\frac{\mathrm{d}\theta}{\mathrm{d}t}\left(\frac{\mathrm{d}\psi}{\mathrm{d}t}\cos\theta + \frac{\mathrm{d}\varphi}{\mathrm{d}t}\right) \tag{2b}$$

$$M_z = I_z\left(\frac{\mathrm{d}^2\varphi}{\mathrm{d}t^2} + \frac{\mathrm{d}^2\psi}{\mathrm{d}t^2}\cos\theta - \frac{\mathrm{d}\psi}{\mathrm{d}t}\frac{\mathrm{d}\theta}{\mathrm{d}t}\sin\theta\right) \tag{2c}$$

The moments M_x, M_y, and M_z are the gas-dynamic moments. The only source of a z moment is the viscous shear between the wall and the azimuthal flow. Therefore, it is zero in inviscid flow and small for viscous flow. In any case this moment has no effect on the coning. If the z moment is neglected then Eq. (2c) has an exact integral

$$\frac{\mathrm{d}\varphi}{\mathrm{d}t} + \frac{\mathrm{d}\psi}{\mathrm{d}t}\cos\theta = \Omega \tag{3}$$

where Ω is the Z-component of angular velocity of the rigid body relative to inertial space. Neglecting the other two moment components gives a free precession solution (valid for constant θ)

$$\frac{\mathrm{d}\psi}{\mathrm{d}t}\cos\theta = \sigma\Omega \tag{4}$$

where the longitudinal-to-transverse inertia ratio, $\sigma = I_z/I$, has been introduced. We are interested in the small gas-dynamic perturbations to this free-precession solution. Further, we note that a nonzero value of the x moment perturbs the precession rate $d\psi/dt$; a positive y moment is unstable and causes the cone angle θ to increase, whereas a negative moment is stable; the z moment changes the total vehicle angular velocity Ω. Because coning is the primary concern the y moment will be of paramount interest here.

In addition to the assumption that the moments are small, we also assume that the cone angle θ is small. A flight vehicle with a large cone angle is a failure; we are interested in the small-angle behavior that may produce such an unsatisfactory state.

With the aforementioned assumptions the expression for the angular velocity becomes

$$\boldsymbol{\omega} = \sigma\Omega\theta\boldsymbol{i}_y + \sigma\Omega\boldsymbol{i}_z \tag{5}$$

We solve three different sets of flow equations: 1) inviscid single phase, 2) inviscid two phase, and 3) viscous single phase. The equations given in this section are general, two-phase viscous flow. The various simplified subsets of equations are obtained by setting the appropriate terms to zero.

The full vector conservation equations for the gas phase in a noninertial reference frame are presented below. They are mass conservation

$$\nabla\cdot(\rho\boldsymbol{v}) = 0 \tag{6}$$

momentum conservation

$$\rho\frac{D\boldsymbol{v}}{Dt} + 2\rho(\boldsymbol{\omega}\boldsymbol{x}\boldsymbol{v}) + \rho\boldsymbol{\omega}\boldsymbol{x}(\boldsymbol{\omega}\boldsymbol{x}\boldsymbol{r}) + \nabla p - \nabla\cdot\tau + G_v^k(\boldsymbol{v} - \boldsymbol{v}_k) = 0 \tag{7}$$

and energy conservation

$$\rho\frac{Dh_T}{Dt} + \rho[2(\boldsymbol{\omega}\boldsymbol{x}\boldsymbol{v}) + \boldsymbol{\omega}\boldsymbol{x}(\boldsymbol{\omega}\boldsymbol{x}\boldsymbol{r})]\cdot\boldsymbol{v} - \nabla\cdot(\tau\cdot\boldsymbol{v}) - \nabla\cdot(K\nabla T) + G_v^k(\boldsymbol{v} - \boldsymbol{v}_k)\cdot\boldsymbol{v}_k + G_h^k(T - T_k) = 0 \tag{8}$$

where for the momentum equation $\boldsymbol{v}$ is the velocity vector in the noninertial frame, $\boldsymbol{r}$ is the position vector of xyz relative to XYZ, p is the static pressure, ρ is the density, τ is the stress tensor, and K is the gas thermal conductivity. The quantity G_v^k is the parameter characterizing the drag between the gas and particle phases and is given by

$$G_v^k = \frac{3\mu\rho_k}{4D_k^2\rho_{pm}}C_d^k Re_k \tag{9}$$

where ρ_{pm} and D_k are the density and diameter of individual particles, respectively. The term ρ_k is the mass per unit volume of the dispersed phase (i.e., ρ_k = number density times particle mass), and $\boldsymbol{v}_k$ is the corresponding particle velocity. The term C_d^k is the particle drag coefficient, and Re_k is the Reynolds number of the particle relative to the gas flow given by

$$Re_k = \frac{\rho D_k|\boldsymbol{v} - \boldsymbol{v}_k|}{\mu} \tag{10}$$

where μ is the gas dynamic viscosity.

In addition, for the energy equation h_T is the total enthalpy in the noninertial frame (i.e., $c_pT + \frac{1}{2}\boldsymbol{v}\cdot\boldsymbol{v}$ where c_p is the gas specific heat), T is the temperature, and the interphase energy exchange parameter G_h^k, is given by

$$G_h^k = \frac{6\alpha_k\rho_k}{D_k\rho_{pm}} \tag{11}$$

where α_k is the heat transfer coefficient associated with the kth particle.

For the particle phase, we have mass conservation

$$\nabla\cdot(\rho_k\boldsymbol{v}_k) = 0 \tag{12}$$

particle momentum conservation

$$\rho_k\frac{D\boldsymbol{v}_k}{Dt} + 2\rho_k(\boldsymbol{\omega}\boldsymbol{x}\boldsymbol{v}_k) + \rho_k\boldsymbol{\omega}\boldsymbol{x}(\boldsymbol{\omega}\boldsymbol{x}\boldsymbol{r}) - G_v^k(\boldsymbol{v} - \boldsymbol{v}_k) = 0 \tag{13}$$

and particle energy conservation

$$\rho_k\frac{Dh_T^k}{Dt} + \rho_k[2(\boldsymbol{\omega}\boldsymbol{x}\boldsymbol{v}_k) + \boldsymbol{\omega}\boldsymbol{x}(\boldsymbol{\omega}\boldsymbol{x}\boldsymbol{r})]\cdot\boldsymbol{v}_k - G_v^k(\boldsymbol{v} - \boldsymbol{v}_k)\cdot\boldsymbol{v}_k - G_h^k(T - T_k) = 0 \tag{14}$$

Rather than solve the equations in the x-y-z space shown in Fig. 3, we solve in the corresponding cylindrical polar coordinates $r\phi z$, with velocities u, v, w. Furthermore, after substituting the value of $\boldsymbol{\omega}$ given in Eq. (5), we linearize in the cone angle θ by taking all dependent variables to be of the form

$$u = u_0 + \theta u_1 \tag{15}$$

This gives two rather lengthy sets of equations[8]: the equations that are zero-order in θ and equations which are first-order in θ. The zero-order equations are a set of nonlinear equations with independent variables r and z, whereas the first-order equations are a system of linear equations with independent variables r, ϕ, and z. For the first-order equations, the ϕ dependence is sinusoidal.[8] Hence, we can represent each dependent variable in the form

$$u_1(r, \phi, z) = Re[U(r, z)\, e^{i\Phi}] \tag{16}$$

Such a substitution for each dependent variable yields a system of equations that is two-dimensional in which each dependent variable has a complex value.

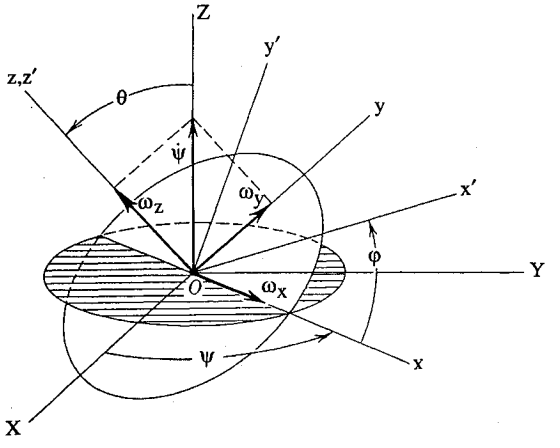

Fig. 3 Coordinate system definition.

III. Inviscid Calculation

The complexity of the geometry and governing equations necessitates a numerical solution. Wang[7] developed a general-purpose program to solve for the flow of single-phase gas for axisymmetric geometries. The program employs a finite-volume approach and the TVD method[9] to ensure high-resolution solutions. The differencing scheme is second-order accurate in space and first-order accurate in time for unsteady problems. Wang's program originally employed an explicit time formulation, but was updated during the course of this work to an implicit one. This update was particularly useful for the steady problems treated here. Grid-generation programs[10] were also developed for mapping complex geometric shapes to the unit square where efficient calculations[11] could be performed. These programs thus served as an excellent starting point for the numerical simulation.

The first task in this numerical analysis was to modify Wang's code to enable the solution of axisymmetric swirling flows in inertial and noninertial reference frames. This addition allowed for the solution of the zero-order equations.[8] The code was next extended to solve the first-order system. Special treatment was required to apply the basic TVD methodology to treat the two-component, complex, dependent variables in the first-order equations.[8] Test cases were performed to validate both the zero- and first-order codes.[8]

To apply the code to the PAM motor, the grain and case geometries are required along with the appropriate boundary conditions. The grain burn-back pattern is presented in Fig. 4 for 1-in. web increments.[12] The innermost configuration is the initial grain shape; numerical solutions were generated at 20, 50 and 80 s into the burn and the corresponding geometries are marked. The grid generated[10] for the 80-s burn-back configuration is presented in Fig. 5. This grid contains 4329 cells and is formed by the intersection of 40 streamwise lines and 112 radial lines.

As for the boundary conditions, the burning solid propellant that forms one boundary is modeled as a stationary surface with mass injection. This surface is a subsonic inflow boundary which requires the specification of four conditions: two tangential velocity components are set to zero; the stagnation temperature is set to 6113°F; and a burn-rate expression relates the normal mass flux and the local static pressure

$$\dot{m}/A = \rho_p \dot{R}(p/p_{\text{ref}})^n \qquad (17)$$

The following values are appropriate for the PAM propellant[13]: propellant density $\rho_p = 0.0651$ lb/in., reference burn rate $\dot{R} = 0.228$ in./s, reference pressure $p_{\text{ref}} = 500$ psia, and burn rate exponent $n = 0.30$. With the boundary conditions and a characteristic formulation described by Murdock,[14] the pressure, density, and normal component of velocity at the boundary, as well as the mass, momentum, and energy fluxes, were computed.

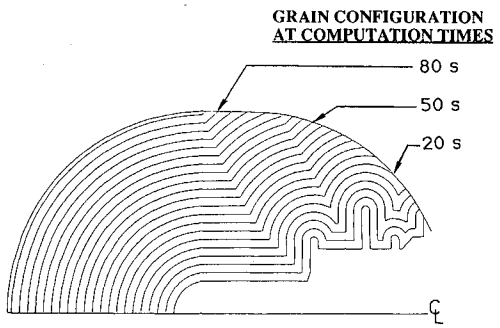

Fig. 4 PAM grain burn-back history.

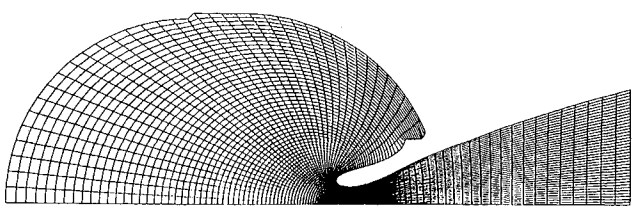

Fig. 5 Grid for 80-s burn-back configuration—inviscid.

The single inviscid boundary condition for the solid wall is that the velocity normal to the surface is zero. This condition was implemented by extending the technique applied by Wang[15] for Cartesian coordinate systems to axisymmetric geometries. The approach is to formulate the momentum equation normal to the wall, require the normal velocity to be zero, and solve the remaining expression for the normal pressure gradient. The wall pressure can then be obtained by spatial differencing.

For axisymmetric flow, the centerline is a coordinate singularity with zero area and, therefore, no boundary condition is required.

For a supersonic exit, no mathematical boundary conditions are necessary. However, to maintain the TVD methodology, two additional columns of cells were generated outside the nozzle's exit plane. For these two columns, the pressure is initially set an order of magnitude smaller than the expected exit pressure, and the values of the other dependent variables are obtained by extrapolating the internal solution field. When the supersonic flow in the divergent nozzle is well-established, the cell pressure for these two added columns is also set by extrapolation.

A gas molecular weight of 29 lb_m/lb_m-mole and a ratio of specific heats γ of 1.16 were chosen for the single-phase simulations.

To apply the first-order code to the PAM motor, the zero-order solution obtained in body-fixed coordinates was transformed to the precessional reference frame defined in Fig. 3. The inertia ratio of the vehicle, which physically defines this transformation, was set to 0.55. The geometry and grids for the zero- and first-order analyses are identical.

Boundary conditions are also necessary for the first-order solution of the PAM motor. The approach was to linearize the boundary routines developed in the zero-order code in the same manner as the governing flow equations. The implementation of these equations followed those of the zero-order solution.

IV. Inviscid Gas-Dynamic Results

For the initial numerical simulation, the geometry corresponded to the grain configuration 80 s into the firing (a time when the motor is unstable) and the motor spin rate was 50 rpm. The results from the zero-order spinning solution are shown in Figs. 6 and 7. Figure 6 is a Mach number contour plot. Chamber Mach number contours are presented from 0.002 to 0.012 at a 0.002 interval. The grain geometry affects the shape of the contour lines with the flow accelerating slowly in the chamber of the motor. Nozzle Mach number contour lines from 0.2 to 4.2 at a 0.4 interval are also displayed. The sonic line occurs near the throat, and two waves are generated by the contoured nozzle. The azimuthal or swirl velocity relative to the motor case is displayed in Fig. 7. Contour lines are displayed from 0 to 20 ft/s at a 5 ft/s interval and between 20–110 ft/s at a 30 ft/s spacing. The swirl velocity increases by about an order of magnitude in the throat region due to conservation of angular momentum.

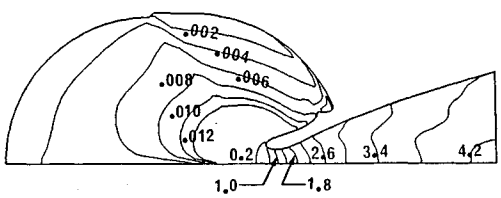

Fig. 6 Mach number contours—80-s inviscid case.

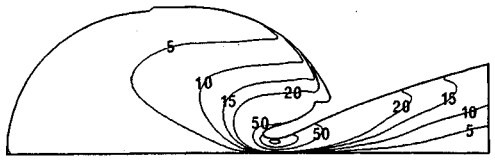

Fig. 7 Azimuthal velocity contours (ft/s)—80-s inviscid case.

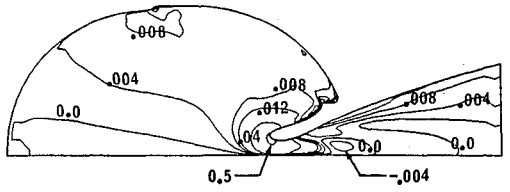

Fig. 8 First-order perturbation pressure contours for 80-s case (psi/rad)—cosine term.

As a check on the accuracy of the solution and the convergence to a steady solution, two quantities that are conserved for steady flow, mass and angular momentum flux were calculated at each cross section formed by the nominally radial grid lines. In the numerical implementation of the steady-state continuity equation, mass should be conserved exactly; mass was conserved to within 0.15%. Conservation of angular momentum flux is implied by the azimuthal momentum equation, but in this case the formulation and the numerics do not force it to be exact; angular momentum was constant within 2.8%.

To calculate the moment determining the growth or decay of the cone angle, the real, or cosine, component of the perturbation (first-order) pressure is required. The imaginary, or sine, component affects the motor's precession rate. A contour plot of the amplitude of the cosine component of the perturbation pressure is presented in Fig. 8. A series of contour lines from -0.004 to 0.012 psi/rad at a 0.004 psi/rad interval, along with two additional contour lines at 0.04 and 0.5 psi/rad are shown. Positive values acting on surfaces that face downward result in stable coning moments; negative values on downward-facing surfaces give unstable moments. A positive perturbation is observed in most regions, with the maximum disturbance occurring near the throat. Integrating the pressures gives a moment per unit cone angle acting about the vehicle's c.m. of -2800 lb_f-in./rad. A negative moment indicates that the gas flow has a stabilizing effect on the vehicle. These calculations take the c.m. of the vehicle to be 108 in. forward of the nozzle exit plane. Convergence of the solution was monitored using techniques similar to those developed for the zero-order code. Since accurate determination of the moment acting on the vehicle is of primary interest, this quantity was plotted against iteration number to ensure its convergence.

The numerically computed moment can be compared with the easily calculated jet-damping moment, in which one-dimensional flow is assumed, i.e., only the axial component of velocity is nonzero. The expression for the jet-damping moment is

$$M_y = -\omega_y \dot{m}(z_2^2 - z_1^2) \tag{18}$$

where ω_y is the transverse, or y-component, of angular velocity, and $\dot{m}$ is the total mass flow rate. The quantities z_2 and z_1 are the nozzle exit and propellant locations of the motor relative to the center of mass, respectively. As stated, z_2 is 108 in. Since the surface of the propellant is curved, z_1 should be found by performing a mass-weighted integral. However, for simplicity we used the smallest and largest possible values of z_1 to bound the jet-damping moment. The distance from the c.m. to the propellant surface at the centerline provides the minimum possible value of z_1. For the 80-s burn-back configuration, z_1 minimum is 29 in. The distance from the center of mass to the end of the propellant where it meets the case wall (53 in.) is z_1 maximum. To compare the jet-damping value with our linearized solution we substitute the expression for ω_y from Eq. (5) to get

$$M_y/\theta = -\sigma\Omega\dot{m}(z_2^2 - z_1^2) \tag{19}$$

The jet-damping moments are -3650 and -4500 lb_f-in./rad for the two bounding values of z_1. Thus, the inviscid model predicts between 62–77% of the jet-damping value.

Table 1 Numeric and jet-damping coning moments

Case	Computer results, lb_f-in./rad	Jet-damping model limits lb_f-in./rad		Ratio computed/ jet-damping
I. Inviscid, single-phase flow coning moments				
20 s, 50 rpm	−1400	−1900	−3400	41–74%
50 s, 50 rpm	−2100	−2900	−4100	51–72%
80 s, 50 rpm	−2800	−3650	−4500	62–77%
50 s, 70 rpm	−3000	−4050	−5750	52–74%
II. Inviscid, two-phase flow coning moments				
80 s, 50 rpm	−3500	−3650	−4500	78–96%
III. Viscous, single-phase flow coning moments				
80 s, 50 rpm	−2800	−3650	−4500	62–77%

In addition to the 80-s burn-back configuration, numerical simulations were performed[8] with the 20- and 50-s motor geometry shown in Fig. 4. The motor spin rate was held at 50 rpm. The results of these simulations are given in Table 1. The coning moments predicted for both the 20- and 50-s configurations have a stabilizing effect on the vehicle. The moment predicted for the 20-s case is about half that predicted for the 80-s configuration, while the 50-s simulation yields a moment about three-quarters the 80-s value. The perturbation pressure distribution in the nozzle is similar for the three geometries considered. The increase in the stabilizing coning moment during the burn is the result of larger positive pressure disturbance in the chamber of the motor.[8] The predicted jet-damping moments for the 20- and 50-s cases are also presented in Table 1. Both the 20- and 50-s simulations predict approximately 60% of the jet-damping value. Thus, geometry has a significant effect on the predicted moment; in contrast to the flight data, the calculations show increasing stability during the firing.

All the analyses up to this point were performed with a motor spin rate of 50 rpm, corresponding to the approximate rate at which motors in previous flights were spun. However, for the Ulysses mission, the PAM-S was designed to operate with a motor spin rate of 70 rpm. Therefore, the effect of increasing the motor spin rate from 50 to 70 rpm was considered by performing a numerical simulation using the 50-s geometry and the higher spin rate. As expected, the higher spin rate results in larger swirl velocities than those present for the 50-rpm spin rate.[8] Higher spin rates also mean larger jet-damping moments as the two quantities are proportional. As reported in Table 1, the first-order analysis predicts about 60% of the jet-damping value. This is approximately the same ratio as calculated for the 50-rpm case. Thus, for the range of spin rates considered, the simulations indicate that the coning moment is proportional to the spin rate, as the simpler jet-damping model also predicts.

V. Two-Phase Flow Analysis

In solid propellant, aluminum is usually added to improve performance. At the surface of the burning propellant the aluminum coalesces and oxidizes forming particles of aluminum oxide. The particles then move away from the propellant surface with the gas flow. However, their finite mass inhibits them from remaining in equilibrium with the local gas veloc-

ity. Hence, the particles begin to deviate from the gas streamlines, which in turn causes the gas flowfield to be altered. Inclusion of the particles was motivated by the fact that the gas flow solution and, hence, the induced moment, would be modified by their presence.

There are two basic approaches for the numerical computation of gas-particle, two-phase flow. In both methods, the gas phase is taken to be a continuum as in the single-phase case. The particle phase may be modeled as a continuum or as a series of discrete particles. For this numerical simulation, the particle phase is treated as a continuum composed of small spheres occupying negligible volume. There are no collisions among particles, and the coupling between the gas and the particle phases is achieved through empirical expressions for the drag and heat transfer of a single sphere in uniform flow given in Sec. II.

In order to compute the coupling terms, expressions for the gas viscosity and thermal conductivity, drag coefficient, and heat transfer coefficient are required. The gas viscosity is a function of temperature. For the two-phase calculation, it is expressed in a power-law form

$$\mu = \mu_0(T/T_0)^{\varepsilon} \tag{20}$$

where ε is equal to 0.65, and the reference viscosity and temperature, μ_0 and T_0, are 1.874×10^{-6} lb_f-s/ft^2 and 6993°R.

The drag coefficient and the heat transfer coefficient are functions of the relative Reynolds number defined in Eq. 10. For our purposes, the relative Reynolds number is small and simple expressions are adapted for the drag coefficient and the Nusselt number. The drag coefficient is divided into Stokes and nonStokes drags[16]:

$$C_d = 24/Re_k \quad \text{for} \quad 0 < Re_k < 0.34$$
$$= 0.48 + 28/Re_k^{0.85} \quad \text{for} \quad 0.34 < Re_k \tag{21}$$

The heat transfer coefficient, expressed in terms of a Nusselt number, is provided by Knudsen and Katz[17]

$$Nu = 2 + 0.6\, PrRe_k \tag{22}$$

where the Prandtl number Pr was taken as 0.72.

To capture the large gradients that exist in the flow,[18–21] the TVD method developed by Harten[9] was applied to both the gas and particle phases. For a system of equations Harten constructs the characteristic form of the equations and then applies his method for a single equation to each of the characteristic equations. In the development of the characteristic equations, eigenvalues and eigenvectors of the system of governing equations are required.[9] However, for the particle phase, the eigenvalues are degenerate, owing to the lack of a quantity corresponding to the pressure in the gas phase. This degeneracy prevents one from obtaining a complete set of independent eigenvectors. Thus, it is not possible to apply the TVD flux modification for the particle system in the same manner as for the gas phase. However, with the exception of the particle continuity equation, the equations for the particle phase are already in characteristic form. Therefore, the TVD flux method is applied to each individual particle equation along the characteristic direction. As for the continuity equation, although not in characteristic form, it is solved along the same characteristic direction as the other equations. A similar approach was taken by Rudinger and Chang[22] when they applied the method of characteristics to two-phase flow. To validate the two-phase code, both one- and two-dimensional test cases were performed.[8]

For the PAM motor appropriate boundary conditions had to be incorporated. The gas phase boundary conditions are identical to those used in the inviscid single-phase simulations. The implementation is also nearly the same. An earlier method[7] was used to calculate the wall pressure in which the wall interaction is treated in terms of one-dimensional wave reflections. Essentially identical results are obtained from both solid-wall boundary condition routines. The inlet boundary was also treated in a slightly different manner as explained below.

For the particle phase, the centerline and downstream boundaries require no conditions and are treated the same as the gas phase. The solid walls are treated as absorbing; any particles that impinge upon the walls are trapped. This condition was implemented by determining (in cells adjacent to the wall) the direction of the particle velocity. If the velocity is toward the wall the particle mass flux at the wall is computed and that mass exits the computational domain. Therefore, the computation correctly models the real PAM motor which traps a finite amount of slag during the burn. A no-flux boundary condition is applied if the particle velocity is away from the wall.

The particle inlet boundary condition is specified such that the particle phase is in thermal and velocity equilibrium with the gas phase.[21] The mass leaving the burn surface is composed of both gas and particles for the two-phase case. In the inlet boundary condition routine described in Sec. III, the burn rate expression [Eq. (17)] represents the total mass flow rate per unit area. It is valid for single- or two-phase flow. For two-phase flow, the fraction composed of particles is determined by the propellant formulation. For the PAM propellant the SPP code[12] predicts that 34% of the mass leaving the surface is in the particle phase. Thus, the mass flow rate is calculated using Eq. (17) and then divided into a gas and a particle portion. The gas flow rate is used to determine the inlet gas conditions in the manner described for the single-phase case.

The values of the gas properties for the single-phase case were selected to simulate the effects of the gas-particle flow. However, for the two-phase case, the gas and particle phases are solved for separately. The gas constant and ratio of specific heats are based on the actual gas composition. The gas composition changes slightly through the motor, but representative values obtained from an SPP run are a gas molecular weight of 20.1 lb_m/lb_m-mole and a ratio of specific heats γ equal to 1.2. In addition, the stagnation temperature was increased from that used in the single-phase cases to a value of 6993°R. This value is higher than the actual stagnation temperature so that our perfect gas model imparts the energy associated with chemical reactions. Hence, the calculated thrust more accurately matches that reported by Morton-Thiokol. The particles were 4 μ in diameter, had a density of 230 lb_m/ft^3, and a specific heat c_p of 11,292 lb_f-ft/slug°R.

The results from the two-phase PAM simulation are presented in Figs. 9–11. The geometry again corresponds to the 80-s configuration, and the motor spin rate is 50 rpm. In order to gain some insight into the two-phase results, the particle density ρ^k is contour plotted in Fig. 9. In the chamber, only the contour line corresponding to $\rho^k = 10^{-1.2}$ $lb/_m/ft^3$ is displayed. Other lines are not shown as the particle density in the chamber varies by only a few percent. In the nozzle, contour lines in the range $10^{-1.5}$–$10^{-3.5}$ lb_m/ft^3 are shown. Clearly evident near the nozzle wall is the particle void region, caused by the inability of the particles to expand with the flow after passing through the nozzle throat. The gas Mach number contour plot is shown in Fig. 10 and is considerably different from the single-phase case (Fig. 6). The maximum

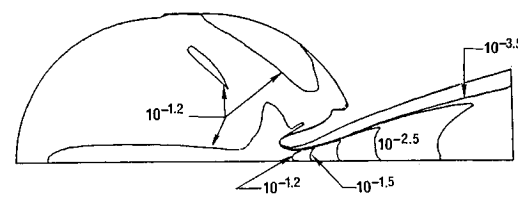

Fig. 9 Particle-phase density contours (lb_m/ft^3).

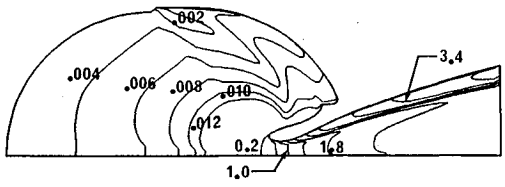

Fig. 10 Gas-phase Mach number contours.

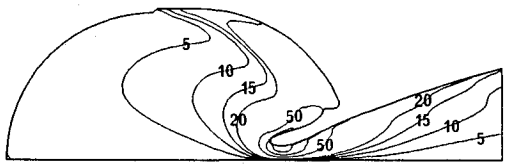

Fig. 11 Gas-phase azimuthal velocity contours (ft/s).

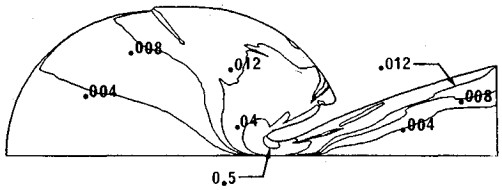

Fig. 12 First-order perturbation pressure contours for two-phase case (psi/rad)—cosine term.

Mach number is shifted from the centerline to near the nozzle wall—the region virtually free of particles. The gas swirl velocity is presented in Fig. 11 and should be compared against the corresponding single-phase case in Fig. 7. Again, the presence of the particles has a significant effect on the distribution; larger swirl velocities are observed in the two-phase case. The particle azimuthal velocity distribution is essentially identical to that of the gas, except in the particle-free region where the particle velocity is undefined.

As in the single-phase case, a code to solve the first-order system of equations was developed. The two-phase first-order equations and the boundary conditions are implemented as described in Sec. III for the single-phase, first-order case. The key result from the simulation is presented in Fig. 12, where the magnitude of the real, or cosine, component of the gas perturbation pressure is presented. For comparison, the single-phase result is shown in Fig. 8. Larger positive perturbation pressures are observed for the two-phase simulation. This increase results in a two-phase moment of -3800 lb_f-in./rad having a more stabilizing effect on the vehicle than the single-phase case, -2800 lb_f-in./rad. The two-phase stabilizing moment represents about 87% of the jet-damping value as summarized in Table 1. Thus, the particles have a stabilizing effect on the vehicle and do not help to explain the observed instability.

VI. Viscous Calculation

If viscous effects result in a large separation region in the imbedded motor chamber, the moment acting on the vehicle may be significantly different than that predicted by the inviscid calculation. The equations governing viscous flow are presented in Sec. II. Viscous effects were considered only for the zero-order solution. With this approach, the separated flow region, which is assumed to be the major effect of viscosity, is still treated. This gives a more expeditious overall treatment.

Widhopf and Wang[11] developed and implemented the basic method used to treat the viscous terms; their technique is used here. To simulate turbulence, the molecular viscosity is replaced by the combination of the molecular and eddy viscosity $\mu + \mu_t$. For the viscous calculations we replaced the power law variation for the dynamic viscosity in the two-phase analysis with a slightly more complicated Sutherland law distribution.[23]

$$\mu = C_1 T^{3/2}/(T + C_2) \tag{23}$$

where C_1 and C_2 are constants taken as 2.269×10^{-8} slug/(ft-s-°R) and 198.72°R, respectively.

Wang and Widhopf[14] showed that the Baldwin-Lomax[24] turbulence model accurately predicts the separated region for external flows. This model was applied to the present internal swirling flow problem. The Baldwin-Lomax algebraic model[24] is divided into two parts: 1) a section to calculate the turbulent viscosity in the so-called inner layer; and 2) a section to determine the outer layer turbulent viscosity. The inner layer scales with the wall shear; the vorticity level in the flow sets the outer layer length scale.

Far from solid boundaries, the turbulent viscosity will be small compared with the molecular viscosity. Therefore, in the majority of the flow the eddy viscosity coefficient was set to zero. The exception was a band along the solid walls of the motor. A fourth-order polynomial in the distance from the wall was used to adjust the distribution so that it smoothly approached zero.

At the burning propellant surface and centerline, the boundary conditions and their implementation remain unchanged from the inviscid case. For the solid walls a no-slip condition is imposed and the walls are assumed to be adiabatic; therefore, the three components of velocity were set to zero and the temperature gradient normal to the wall is zero. The wall temperature was obtained by finite-differencing the expression for the normal temperature gradient. Application of the no-slip condition to the continuity equation yields the wall density, and the wall pressure follows from the ideal gas law. Wall fluxes are calculated from the boundary values.

At the exit plane, the flow is supersonic except for a small region in the boundary layer. From a mathematical standpoint, boundary conditions at the outflow are required. However, the effect of these conditions is confined to a layer of thickness $O(Re^{-1})$. Thus, from a practical standpoint, there is no upstream influence except in the boundary layer (where $Re \to 0$). We impose no boundary conditions except extrapolation at any supersonic downstream station. For the subsonic boundary-layer region experience has shown that for high-speed flows of the type considered here, the upstream effect is minimal. Therefore, the same extrapolation technique employed for the inviscid cases was employed in the viscous analysis.

The grid used in the inviscid calculation was not adequate to resolve the boundary layer or any recirculation region that may exist. Therefore, a new grid for the 80-s burn-back geometry was generated[25] with cells densely packed near the solid walls where the turbulence level is known to be large. In the initial viscous grid, the boundary layer at some locations along the wall was not completely resolved. Therefore, a series of grids was generated until a grid was found in which a minimum of five or six points were within the laminar sublayer. Additional grid lines were added so that the resolution in the interior of the motor was not compromised. The final grid consisted of 8509 cells, almost twice as many as were used in the inviscid case. The grid contains 68 streamwise grid lines and 128 radial lines.

The Mach number and azimuthal velocity distributions from the turbulent simulation are nearly identical to their inviscid counterparts (Figs. 6 and 7). An exception is the thin boundary layer along the walls of the motor for the viscous case. In addition, two recirculation regions are present in the very corner of the chamber, but both are extremely small.[8]

The first-order perturbation pressure about the zero-order turbulent flowfield is nearly identical to that obtained from the inviscid calculation (Fig. 8). A stabilizing moment of -2800 lb_f-in./rad was obtained, which is the same value as that pre-

dicted for the inviscid case. Therefore, the inclusion of the turbulent, viscous terms in the zero-order solution has only a small effect on the perturbed flowfield.

VII. Conclusion

An inviscid simulation was performed with geometry corresponding to the grain configuration 80 s into the burn and a motor spin rate of 50 rpm. A stabilizing moment of -2800 lb_f-in./rad was predicted, which represents about 70% of the jet-damping value. Thus, although the simulation results in a moment smaller than the jet-damping value, stability is predicted.

Two additional configurations, which correspond to the burnback geometries 20 and 50 s into the firing, were analyzed. Stabilizing moments of -1400 and -2100 lb_f-in./rad are calculated, respectively. Thus, the geometry has a significant effect on the moment. However, in contrast to the flight data, the simulation predicts greater stability later in the burn. These moments are about 58 and 62% of their jet-damping values. A second, higher motor spin rate case was also considered. Results indicate that in the range of spin rates considered, the moment was proportional to spin rate. The simpler jet-damping model also predicts this behavior.

Separate inclusion of the solid particles and the fluid viscosity in the model did not change the conclusions reached in the inviscid, single-phase computations. For the 80-s burnback geometry, the two-phase flow calculation yields a larger stabilizing moment than the inviscid case, -3800 lb_f-in./rad. The turbulent simulation for the 80-s geometry predicts a moment nearly equal to that of the inviscid solution. Thus, the analysis indicates that the gas-dynamic flow is not the cause of the observed coning instability.

References

[1]Thomson, W. T., and Reiter, G. S., "Jet Damping of a Solid Rocket: Theory and Flight Results," *AIAA Journal*, Vol. 3, No. 3, 1965, pp. 413–417.

[2]Meyer, R. X., "Convective Instability in Solid Rocket Motors," *Advances in the Astronautical Sciences*, edited by G. T. Tseng, Vol. 54, Pt. II, AA583-368, Univet Inc., San Diego, CA, 1984, pp. 657–669.

[3]Murdock, J. W., and Meyer, R. X., "The Stability of a Precessing Vehicle with Outflow," Aerospace Corp., Rept. TR-089(446406)-1, Los Angeles, CA, April 15, 1991.

[4]Flandro, G. A., Van Moorhem, W. K., Shorthill, R., Chen, K., Woosley, M., Clayton, C. D., and Findlayson, P. A., "1986 Fluid Mechanics of Spinning Rocket Motors," USAF Rocket Propulsion Lab., Rept. AL-TR-86-072, Edwards AFB, CA, Sept. 1986.

[5]Flandro, G. A., Leloudis, M., and Roach, R., "Flow Induced Nutation Instability in Spinning Solid Propellant Rockets," Astronautics Lab. (AFSC), Rept. AL-TR-89-084, Edwards AFB, CA, Sept. 1986.

[6]Roach, R., Barnley, V., Flandro, G., and Burnette, J., "Internal Ballistics Interactions in Spinning Rocket Nutation Instability," AIAA Paper 90-0042, Jan. 1990.

[7]Wang, J. C. T., and Widhopf, G. F., "A High Resolution TVD Finite Volume Scheme for the Euler Equations in Conservation Form," AIAA Paper 87-0538, Jan. 1987.

[8]Misterek, D. L., Murdock, J. W., and Koshigoe, S., "The Analysis and Simulation of the PAM-S Coning Instability—Vol. 4. Analysis of Gas Dynamics," Aerospace Corp., Rept. TOR-0091(646406)-1, Los Angeles, CA, Sept. 30, 1990.

[9]Harten, A., "High Resolution Schemes for Hyperbolic Conservation Laws," *Journal of Computational Physics*, Vol. 49, No. 3, 1983, pp. 357–393.

[10]Thompson, J. F., Warsi, Z. U. A., and Mastin, C. W., *Numerical Grid Generation—Foundations and Applications*, Elsevier, New York, 1985, pp. 454–459.

[11]Widhopf, G. F., and Wang, J. C. T., "A TVD Finite Volume Technique for Nonequilibrium Chemically Reacting Flows," AIAA Paper 88-2711, June 1988.

[12]Nickerson, G. R., Culick, F. E. C., and Dang, A. L., "The Solid Propellant Rocket Motor Performance Computer Program (SPP) Version 6.0," AFAL-TR-87-078, Edwards AFB, CA, Dec. 1987.

[13]*Star Rocket Motor Catalog*, Morton Thiokol, Inc., Elkton Div., Elkton, MD, Jan. 1987.

[14]Murdock, J. W., "Rocket Thrust Perturbation from Discharge of an Inert Body," *Journal of Propulsion and Power*, Vol. 2, No. 2, 1986, pp. 117–123.

[15]Wang, J. C. T., and Widhopf, G. F., "An Efficient Finite Volume TVD Scheme for Steady State Solutions of the 3-D Compressible Euler/Navier-Stokes Equations," AIAA Paper 90-1523, June 1990.

[16]Gilbert, M., Davis, L., and Altman, D., "Velocity Lag of Particles in Linearly Accelerated Combustion Gases," *Jet Propulsion*, Vol. 25, Jan. 1955, pp. 26–32.

[17]Knudsen, J. G., and Katz, D. L., *Fluid Mechanics and Heat Transfer*, McGraw-Hill, New York, 1955, p. 511.

[18]Hwang, C. J., and Chang, G. C., "Numerical Study of Gas-Particle Flow in a Solid Rocket Nozzle," *AIAA Journal*, Vol. 26, No. 6, 1988, pp. 682–689.

[19]Golafshani, M., and Loh, H., "Computation of Two-Phase Viscous Flow in Solid Rocket Motors Using a Flux-Split Eulerian-Lagrangian Technique," AIAA Paper 89-2785, July 1989.

[20]Hayashi, K., Matsuda, M., Fujiwara, T., and Arashi, K., "Numerical Simulation of Gas-Solid Two-Phase Nozzle and Jet Flows," AIAA Paper 88-2627, June 1988.

[21]Chang, I. S., "One- and Two-Phase Nozzle Flows," *AIAA Journal*, Vol. 18, No. 12, 1980, pp. 1455–1461.

[22]Rudinger, G., and Chang, A., "Analysis of Nonsteady Two-Phase Flow," *Physics of Fluids*, Vol. 7, No. 11, 1964, pp. 1747–1754.

[23]Anderson, D. A., Tannehill, J. C., and Pletcher, R. H., *Computation of Fluid Mechanics and Heat Transfer*, Hemisphere, New York, 1984, pp. 189.

[24]Baldwin, B. S., and Lomax, H., "Thin Layer Approximation and Algebraic Model for Separated Flows," AIAA Paper 78-257, Jan. 1978.

[25]Thompson, J. F., *Program EAGLE Numerical Grid Generation System User's Manual*, Vols. I–III, AFATL-TR-87-15, March 1987.